

Interfaces in *REBCO*-Based Nanocomposite Thin Films and their Contribution to Vortex Pinning



Alok K. Jha and Kaname Matsumoto

1 Interfaces and their Structures

An interface may be termed as a small number of atomic layers which separate two different crystalline solids in contact with each other [1]. For example, a thin film deposited on a crystalline substrate is separated by the substrate-thin film interface. Another example could be the interfaces inside a superconducting film which separate the superconducting matrix and non-superconducting inclusions. The property at the so-called interface is very much different from the crystalline solids it separates [2].

Interfaces are broadly classified into two types: (i) homophase interfaces and (ii) heterophase interfaces. An interface separating two regions of the same phase is called a homophase interface which is often termed as a grain boundary. An interface separating two different crystal phases is called a heterophase interface [3].

Interfaces are also classified in other three classes based on their structural features. These are called (i) coherent, (ii) semi-coherent, and (iii) incoherent interfaces. Starting with a reference structure and making a series of operations, these interfaces can be constructed exhibiting different structural features [4].

Figure 1 shows the construction of a heterophase interface between two different crystal phases: phase 1 and phase 2. The reference structure is the single crystal of phase 1. The dashed line in Fig. 1a indicates the location of the interface to be constructed. The first operation transforms the upper portion of the crystal 1 into phase 2 while maintaining registry along the interface as shown in Fig. 1b. As the two phases (1 and 2) adjoining the interface are maintained in the registry, the resulting

A. K. Jha (✉) · K. Matsumoto

Department of Materials Science and Engineering, Kyushu Institute of Technology,
Kitakyushu, Japan

e-mail: akjha@post.matsc.kyutech.ac.jp

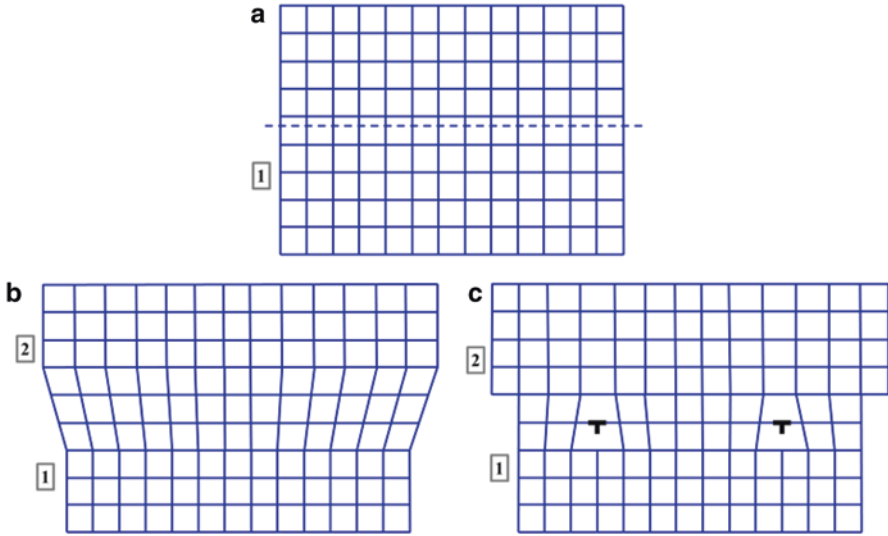


Fig. 1 Schematic diagram of a heterophase interface. (a) Phase 1 is the reference crystal. (b) Transformation of the upper region of the interface into phase 2 while maintaining coherence. (c) Relaxation of long-range stresses by the introduction of dislocations at the interface between the phases

interface is coherent. In order to maintain the interface registry, long-range coherency stresses are required.

The formation of a semi-coherent interface requires another operation in which these stresses are eliminated by introducing some dislocations in the interface as represented in Fig. 1c. Thus the resulting interface consists of patches of coherent interface separated by dislocations. In this process, the overall coherence of the interface is destroyed by the cuts and displacements resulting in dislocations, and such an interface is, therefore, considered to be semi-coherent with respect to the reference structure in Fig. 1a.

If the density of the dislocation is so large that their cores overlap, then the coherence characteristics of the reference structure will be destroyed, and it will result in an incoherent interface. The cores of incoherent interfaces, therefore, consist of continuous slabs of poor material, and the interfaces lack long-range order.

In REBCO-based nanocomposite thin films, vortex pinning and subsequently critical current densities tend to be sensitive to not only the geometry and concentration of nanoscale inclusions but also to the interfacial composition and the resulting nanoscale lattice defects.

2 REBCO Superconductors and their Critical Parameters

Superconductivity in $\text{YBa}_2\text{Cu}_3\text{O}_{7-\delta}$ (YBCO) was first discovered in its bulk polycrystalline form and the superconducting transition was observed above the liquid nitrogen temperature (77 K) [5]. The discovery of YBCO accelerated the search for higher transition temperature (T_c) materials and in the quest of discovering higher T_c superconductor, other rare-elements were tried to replace Y in YBCO [6–8]. Apart from the critical temperature (T_c) and critical magnetic field (H_c), the critical current density (J_c) is the most relevant parameter of a superconductor which determines the practical utility of a superconductor [9–11].

Soon after the discovery of REBCO superconductors in their polycrystalline forms, it became possible to make their thin films on single crystal substrates such as SrTiO_3 , Al_2O_3 , MgO , *etc.* [12–14]. The current carrying capability of REBCO superconducting thin films significantly enhanced over the years due to the development of the fabrication and processing techniques. Many fabrication techniques such as pulsed laser deposition (PLD) [15], chemical solution deposition (CSD) [16], metal organic chemical vapor deposition (MOCVD) [17] have been developed over the years to deposit high quality oriented REBCO thin film which exhibit high J_c of 1–5 MA/cm² at 77 K, self-field [18, 19].

3 Vortex Pinning by APCs in REBCO Thin Films

In the critical state of a type-II superconductor (such as REBCO), the flow of electrical current is limited by temperature and applied magnetic field. When an electrical current is passed across a superconducting sample subjected to an applied magnetic field, the vortices experience a Lorentz force in a direction perpendicular to both the current and the applied magnetic field as depicted in Fig. 2. The movement of the vortices due to Lorentz force would generate an electric field leading to energy dissipation. The vortices, therefore, need to be pinned at their respective locations inside the superconducting matrix [20].

Some microscopic defects are naturally generated during the growth of thin films, such as grain boundaries, oxygen vacancies, point defects, dislocations, *etc.* Some of these defects act as pinning centers for vortices against the Lorentz force. Figure 3 shows the schematic diagram of such naturally generated defects in a typical superconducting REBCO thin film. These naturally generated pinning centers, however, are not strong enough to prevent the vortex motion under applied magnetic fields at elevated temperatures [11, 21, 22].

An alternative strategy employed to prevent the motion of the vortices is the generation of artificial defects inside superconducting matrix. Such intentionally generated pinning centers are termed as artificial pinning centers (APCs). The APCs are introduced into REBCO films through different methods which include addition and/or substitution of rare-earth atoms [23, 24] or incorporation of nanoscale

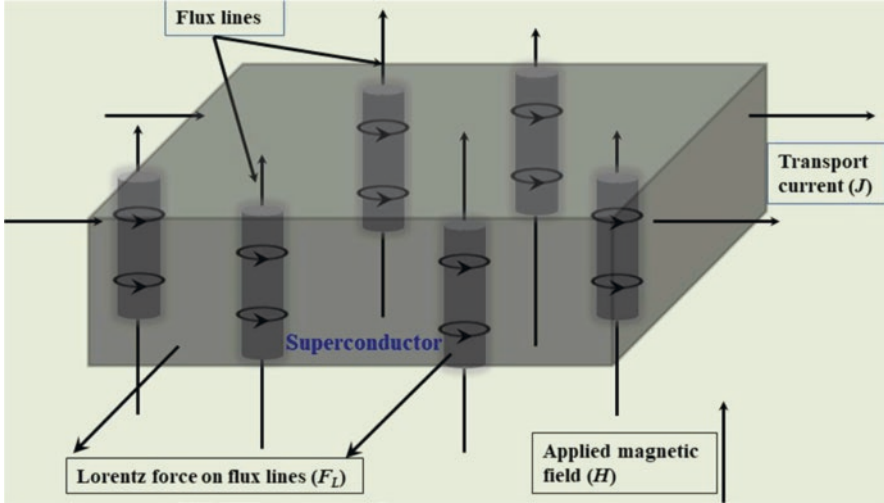


Fig. 2 The mixed state in a type-II superconductor. Magnetic flux starts penetrating the sample in the form of vortices, with quantized flux $\Phi_0 = h/(2e)$. (Reproduced from Jha and Matsumoto [20])

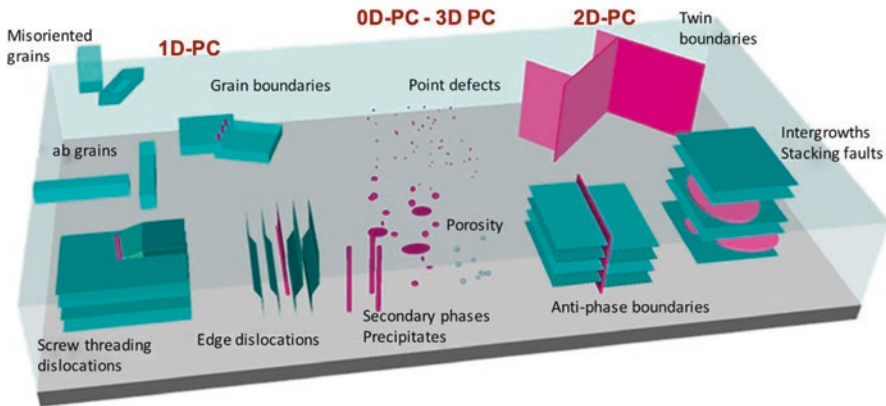


Fig. 3 Schematic diagram of various defects generated during the growth of *REBCO* thin films. The ones shown in pink are useful for vortex pinning whereas others are detrimental to the superconducting properties. (Reproduced from Palau et al. [60])

secondary phases into the *REBCO* film matrix [25–37] or decoration/modification of the substrate surface [38, 39]. Improved vortex pinning in *REBCO* films through incorporation of secondary phase nano-inclusions has been frequently observed. These secondary phases are self-assembled either in the form of nanocolumns or nanoparticles inside the *REBCO* matrix as represented in the schematics in Fig. 4. The nanoscale inclusions of secondary phases such as Y_2BaCuO_5 [25, 26], Y_2O_3 [27], BaTiO_3 [28], BaZrO_3 [29–31], BaSnO_3 [32, 33], BaHfO_3 [34], YBa_2NbO_6 [35, 36], and YBa_2TaO_6 [37] have been successfully observed to enhance the in-field J_c of *REBCO* thin films over a wide range of temperature and applied magnetic field.

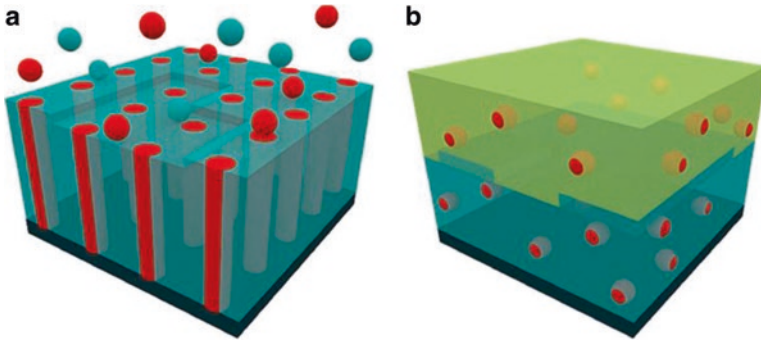


Fig. 4 The schematic diagram representing the formation of (a) columnar and (b) spherical nanostructures with simultaneous and sequential nucleation of secondary phases and the REBCO matrix, respectively. (Reproduced from Palau et al. [60])

4 Interfaces in REBCO Thin Films Consisting of Columnar Nanostructures (1D APCs)

Several secondary phase materials, when incorporated into the REBCO thin films, tend to self-assemble in the form of nanocolumnar structures running through the thickness of the thin films. Because of their orientation along a particular direction (along the c -axis of REBCO), they are also termed as one-dimensional (1D) APCs. Several perovskite and double-perovskite materials such as BaZrO_3 [29–31], BaSnO_3 [32, 33], BaHfO_3 [34], *etc.*, have been observed to self-assemble in the form of nanocolumnar structures inside REBCO films. These nanocolumns have been successfully observed to enhance the in-field J_c of REBCO thin films over a wide range of temperature and applied magnetic field.

In analogy to H_c of a superconductor, irreversibility field (H_{irr}) is another very important parameter which is defined as the magnetic field at which the vortex pinning strength become negligibly small due to large resistivity values caused by the vortex motion [40, 41]. The irreversibility line separates H - T phase diagram of a superconductor into reversible and irreversible (or hysteretic) portions. In the reversible portion of this H - T phase diagram, the vortex movements due to thermal fluctuation are so large that the ordered vortex lattice state is destroyed [42, 43]. It is highly desired to shift this irreversibility line towards higher H - T regime by artificial pinning center (APC) technology [9, 11, 44, 45] and many reports have successfully addressed this issue by introducing nanocolumnar structures inside REBCO thin films.

In a recent work, Horii et al. [46] have successfully introduced columnar nanostructures of Ba-Nb-O (BNO) phase inside YBCO thin films. In this study, it has been estimated that a lower T_c matrix annulus with a lateral dimension of ~ 12 – 14 nm exists around each BNO nanocolumns resulting from the strong interface strains. The generation of lower T_c region around the BNO nanocolumns enhances vortex pinning significantly.

Figure 5 shows the schematic diagram of the interfaces (cross-sectional view) in the YBCO films consisting of BNO nanocolumns. In this figure, d , l , and D represent the average diameter of the BNO nanocolumns, distance from the YBCO/BNO interface of a relatively lower T_c region, and average inter-columnar distance. According to their model, it is suggested that stronger vortex pinning is expected for $D > 2l+d$, and a significant reduction of vortex pinning is apparent for $D \leq 2l+d$.

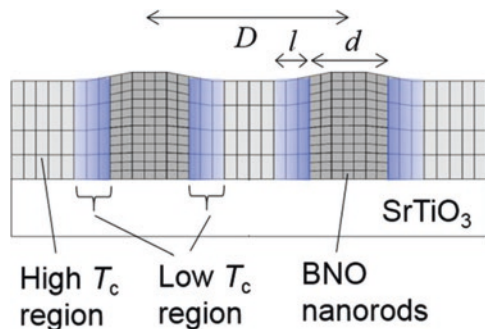
The generation of the lattice strain in the YBCO matrix by incorporating BNO nanocolumns was ascertained by calculating the c -axis lengths from reciprocal space measurement (RSM). The RSM measurements confirmed the coexistence of the a - and b -axes of the YBCO film, which is induced by twin microstructures parallel to the surface of the STO substrate. Whereas the same could not be observed for the YBCO film incorporating BNO nanocolumns which suggested that the broadening of the diffraction spots in the YBCO matrix is apparently induced by the introduction of the BNO nanocolumns.

Figure 6 shows the comparison of the irreversibility field of pristine YBCO and YBCO+BNO nanocomposite films with varying concentrations of BNO phase. It can be clearly observed that the irreversibility lines for YBCO films with BNO nanocolumns were clearly shifted toward higher H - T regions by BNO incorporation, and the vortex-glass region became qualitatively larger with the increase in the nominal BNO concentration [47–49]. It is well known that the H_{irr} value is correlated with the magnitude of vortex pinning energy through the change in electromagnetic anisotropy in high- T_c cuprate superconductors [50, 51]. It was suggested in their study that all the YBCO matrix regions are dominated by the lower T_c regions, which is induced by the lattice strain at the nanorod/matrix interface.

The incorporation of BZO and BSO nanocolumns into ErBCO and SmBCO thin films has also been reported due to which strong enhancement in the in-field J_c has been observed [52, 53]. The role of interfaces although was not highlighted in these studies.

The incorporation of a double-perovskite phase YBNO has been reported to achieve extremely high pinning force density (F_p) values in YBCO thin films [54]. The YBNO nanocolumns were observed to grow along the c -axis of the YBCO film. The continuous nanocolumns also exhibited some segmentation, and the distortions arising from stacking faults in the YBCO matrix near the YBCO/YBNO interface

Fig. 5 Schematic diagram of the cross-sectional view of an YBCO film with BNO nanocolumns. The strained regions near the interfaces have their T_c s reduced. (Reprinted from Horii et al. [46], with the permission of AIP Publishing)



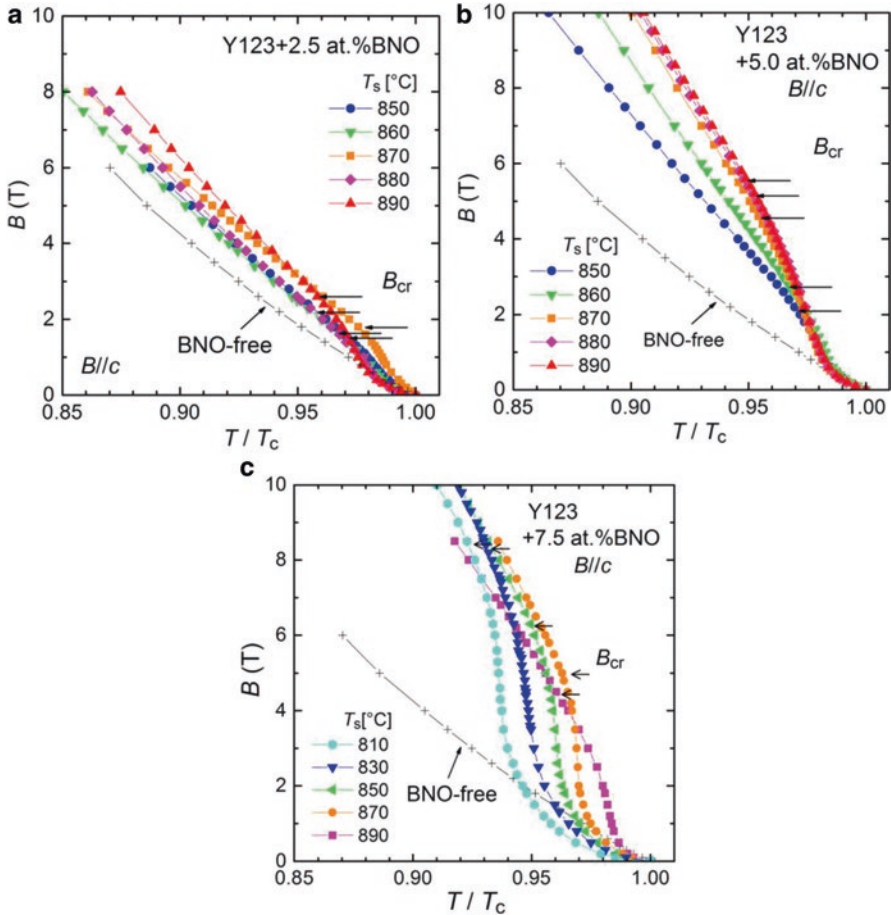


Fig. 6 Variation of irreversibility field for YBCO films with varying concentrations of BNO (a) 2.5%, (b) 5%, and (c) 7.5% deposited at different substrate temperatures. (Reprinted from Horii et al. [46], with the permission of AIP Publishing)

were also observed. A thin layer of amorphous material was observed at these points which are important as they provide a mechanism to release the lattice strain resulting from the large lattice misfit between the phases.

Recently, Cantoni et al. [55] have reported that the strain-induced oxygen-deficient matrix regions exist at YBCO/BZO interfaces, and the distance of such regions from the interface is ~ 10 nm in an YBCO film with BZO nanocolumns. Figure 7a shows the cross-sectional view of the YBCO/BZO (4 vol%) nanocomposite film. BZO phase can be observed in the form of c -axis oriented nanocolumns which is common in YBCO/BZO films grown by PLD technique. The lattice misfit occurs between BZO and YBCO phases along the vertical interfaces. The distribution of the out-of-plane strain has been calculated in this study which results from

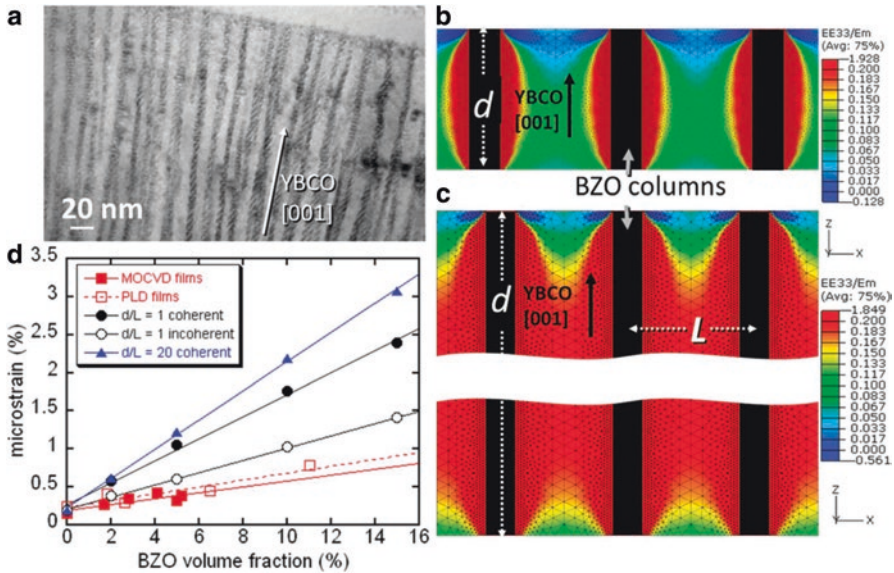


Fig. 7 (a) Cross-sectional TEM image of an YBCO/BZO nanocomposite film. Volumetric average of the out-of-plane strain calculated from FEM calculations for the cases $d/L = 1$ (b) and $d/L = 20$ (c). (d) Variation of microstrain versus BZO concentration as calculated by the FEM method for the cases $d/L = 20$ coherent interface (blue triangles), $d/L = 1$ coherent interface (black dots), $d/L = 1$ incoherent interface (black circles), and measured by XRD for PLD films (open squares) and MOCVD films (filled squares). (Reproduced from Cantoni et al. [55])

this misfit using the finite element method (FEM) which is shown in Fig. 7b, c for two different values of the ratio between nanocolumn length, d , and inter-column distance L , representing low and high concentrations of BZO nanocolumns in the YBCO matrix, respectively. It was found that high concentration of BZO nanocolumns results in a larger overall positive strain of the YBCO along the c -axis causing elongation of the c -axis. Figure 7d shows the variation of microstrain as a function BZO concentration as calculated from the Williamson-Hall plot of the XRD data. It can be observed that the microstrain also increases with increasing BZO concentration. The comparative results indicated that the experimental value is significantly reduced in comparison to the simulated value for the case of $d/L = 20$ and coherent interface, which indicate that much of the lattice strain has been relieved through misfit dislocations that are generated at the YBCO/BZO interface, giving rise to a semi-coherent YBCO/BZO interface.

The HRTEM image of such an interface is shown in Fig. 8. In Fig. 8b, large number of defects, such as dislocations, can be observed which are marked with white arrows. The high-resolution Z-STEM micrograph of the BZO nanocolumn in Fig. 8a is shown in Fig. 8b which reveals that the BZO c -axis and the REBCO c -axis are tilted with respect to each other by nearly 3° . This commonly observed tilt is accommodated by tilt dislocations as marked by circles. The misfit dislocations are

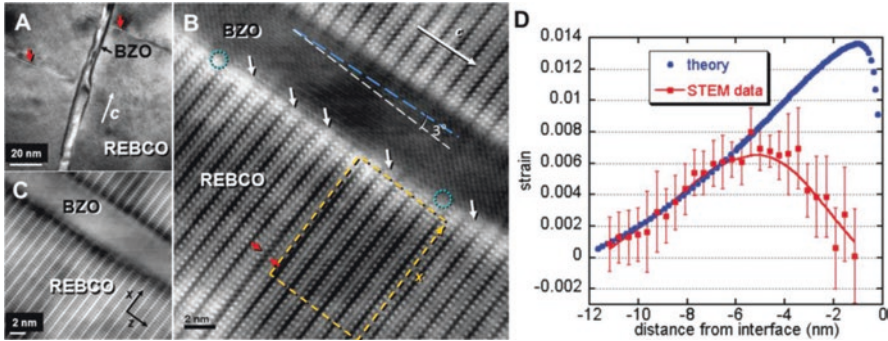


Fig. 8 (a) TEM image of a BZO nanocolumn inside REBCO matrix. (b) High-resolution Z-STEM image of the same nanocolumn in (a). Light blue circles indicate pure tilt dislocations and white arrows indicate misfit dislocations. (c) Bright field image acquired simultaneously to image (b). (d) Comparison between theoretically calculated and experimentally measured strain. (Reproduced from Cantoni et al. [55])

also revealed in this image which are effective in relieving the lattice strain (arrows in Fig. 8b).

The local strain has been quantified through the Z-STEM images by measuring the variation of the REBCO *c*-axis lattice parameter. Figure 8d shows the comparison between theoretically calculated strain (blue dots) and experimentally measured strain (red squares). It has been observed that the strain increases when moving from the matrix interior toward the BZO nanocolumn until it reaches a peak value at a distance of ~5 nm from the interface. However, near the BZO interface, the strain decreases rapidly over a distance of ~3 nm. In the narrow REBCO strip, where the tilt and misfit dislocations cause strong lattice distortions, both compressive and tensile strain components result in atomic displacements along the columns. The analytical prediction of the local strain distribution near the YBCO/BZO boundary is also shown in Fig. 8d. The observed peak of the measured strain separates two concentric YBCO columns with widely varying *T_c*s. The defective YBCO column (closer to the boundary) has been found to be highly oxygen deficient, which is expected to have a much lower *T_c* than the *T_c* of the YBCO phase which exist on the another side of the strain peak.

The role of REBCO/APC interface in improving vortex pinning has further been highlighted in a recent work by Gautam et al. [56]. In this study, they have made two different kinds of nanocomposites: YBCO+BZO and YBCO+BHO. Both BZO and BHO phases tend to form nanocolumns inside REBCO matrix prepared by PLD and MOCVD techniques. These *c*-axis oriented nanocolumns or the so-called 1D APCs have proven to provide strong correlated pinning of vortices resulting in enhanced in-field *J_c* in superconducting YBCO films. Although, there has always been discussions on the issue as to what would fundamentally determine the pinning efficiency of different 1D APCs. Both BHO and BZO phases were observed to have similar lateral dimensions of 5–6 nm. Figure 9a, b, c shows the cross-sectional TEM image of YBCO+BZO and YBCO+BHO nanocomposite films in which the formation of

nanocolumns can clearly be observed. The corresponding Fourier filtered images of these films are also shown in Fig. 9d, e, f. While comparing the Fourier filtered images of both YBCO+BZO and YBCO+BHO nanocomposite films, it was observed that there is larger number of dislocations along the YBCO/BZO interface which the authors have attributed to the larger lattice misfit between YBCO and BZO phases as compared to that between YBCO and BHO phases. In contrast, the YBCO/BHO interface was observed to be coherent, although a few randomly distributed dislocations and significant *ab*-plane buckling was also observed. The high interfacial defect concentration in the YBCO+BZO films is attributed to the release of strain in a short range of 1–2 nm from the interface, where oxygen deficiency was earlier found to be significant [55].

Figure 10 shows the variation of J_c and F_p with respect to applied magnetic field for YBCO+BZO and YBCO+BHO nanocomposite films measured at 77 K and 65 K. The in-field J_c values of the YBCO+BHO nanocomposite films are much higher than their BZO counterpart which is reflected in much higher F_{pmax} values of YBCO+BHO films (182 GNm^{-3} at 65 K). The authors have attributed the highly enhanced vortex pinning properties of YBCO+BHO films to a highly coherent YBCO/BHO interface. The coherent nature of the YBCO/BHO interface is attributed to the smaller lattice misfit between YBCO and BHO phases which would allow BHO and YBCO lattices to compromise to each other due to low rigidity of the BHO nanocolumns. In contrast, the BZO nanocolumns are prone to the interface defects, resulting in a semi-coherent YBCO/BZO interface.

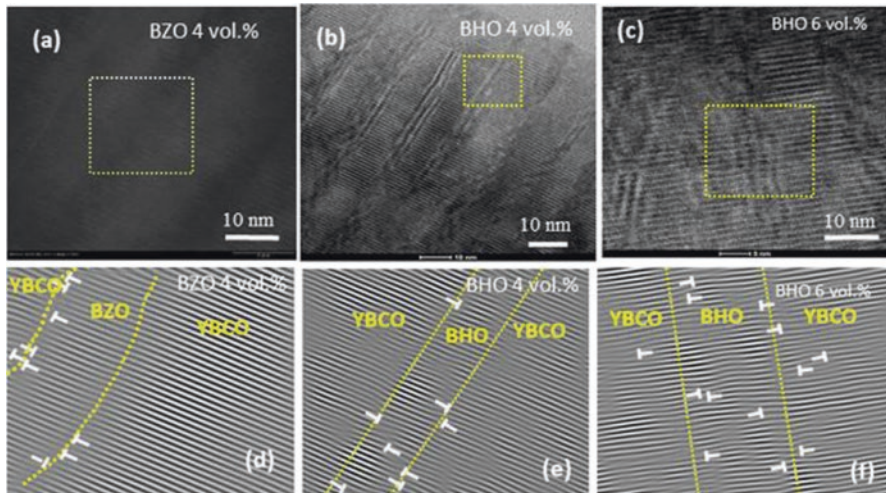


Fig. 9 Cross-sectional HRTEM images of YBCO nanocomposite films consisting of (a) 4 vol.% BZO, (b) 4 vol.% BHO and (c) 6 vol.% BHO. The corresponding Fourier filtered images of the marked areas (rectangles) in (a), (b), and (c) are shown in (d), (e), and (f) respectively. (Reprinted from Gautam et al. [56], with the permission of AIP Publishing)

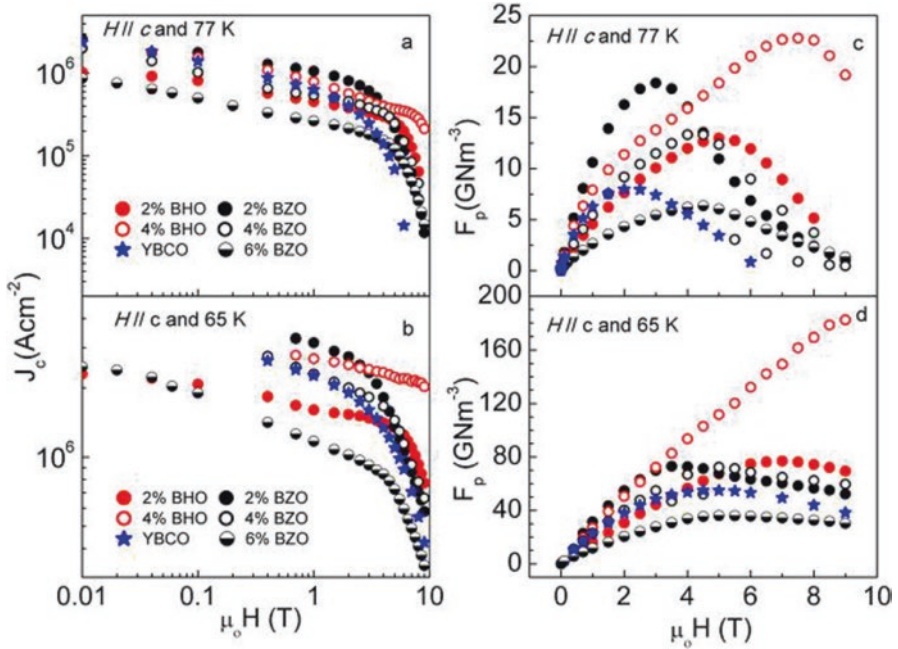


Fig. 10 Variation of J_c and F_p with applied magnetic field for pristine YBCO film in comparison to YBCO films with varying concentrations of BZO and BHO nanocolumns. These data are obtained for ($H//c$ -axis) at 77 K (a) and (c) and at 65 K (b) and (d). (Reprinted from Gautam et al. [56], with the permission of AIP Publishing)

5 Interfaces in REBCO Thin Films Consisting of Spherical Nanostructures (3D APCs)

The secondary phase materials when incorporated inside REBCO film matrix exhibit different geometries which depend upon many parameters. Lattice misfit between the phases and surface diffusion co-efficient of adatoms are crucial in determining the interface between the two phases which may be coherent, semi-coherent, or incoherent [57]. The surface energies of coherent and semi-coherent interfaces are much lower in comparison to that of the incoherent interfaces and the large surface energies of the incoherent interfaces result in coarsening of the grains in polycrystalline films [58] and faceting of precipitates and grain boundaries [1]. It has also been reported that the morphology of the secondary phase nanoinclusions inside REBCO matrix is determined by the combined effect of lattice misfit and elastic properties of REBCO and secondary phase materials [59].

The morphology or geometry of the secondary phase nanoinclusions is also determined by the growth or deposition techniques [60]. For example, in-situ growth techniques such as pulsed laser deposition (PLD), chemical vapor deposition (CVD), or hybrid liquid phase epitaxy (HLPE) allow simultaneous nucleation and

growth of the *REBCO* and secondary phases which result in self-assembled nanostructures, such as nanocolumns of the secondary phases oriented along the *c*-axis. These secondary phase nanoinclusions are in contact with the *REBCO* phase through coherent or semi-coherent interfaces. Chemical solution deposition (CSD) technique, on the other hand, results in *REBCO* films consisting of nanoscale secondary phases which are formed in a precursor film in which nucleation and growth of the *REBCO* matrix is delayed. The secondary phase nanoinclusions remain trapped during the *REBCO* growth and they are randomly oriented within the superconducting film matrix [57, 61]. During the growth of the *REBCO* phase, these randomly oriented nanoparticles induce a high density of stacking faults in the resulting film to relieve the strain at the incoherent interfaces. The nanostrained regions surrounding the stacking faults have been suggested to be very efficient in inducing isotropic core pinning due to Cooper pair suppression [61, 62].

Figure 11 shows the nanostructural view of YBCO+BZO and YBCO+YBTO nanocomposite films prepared from CSD technique as reported by Palau et al. [60]. These nanocomposite films are highly strained with a large number of stacking faults in the YBCO phase. These defects and the associated distortions in the YBCO matrix [63] have been suggested to be efficient isotropic weak pinning sites and a large density of such short stacking faults improve the isotropic weak pinning contribution in YBCO nanocomposite thin films.

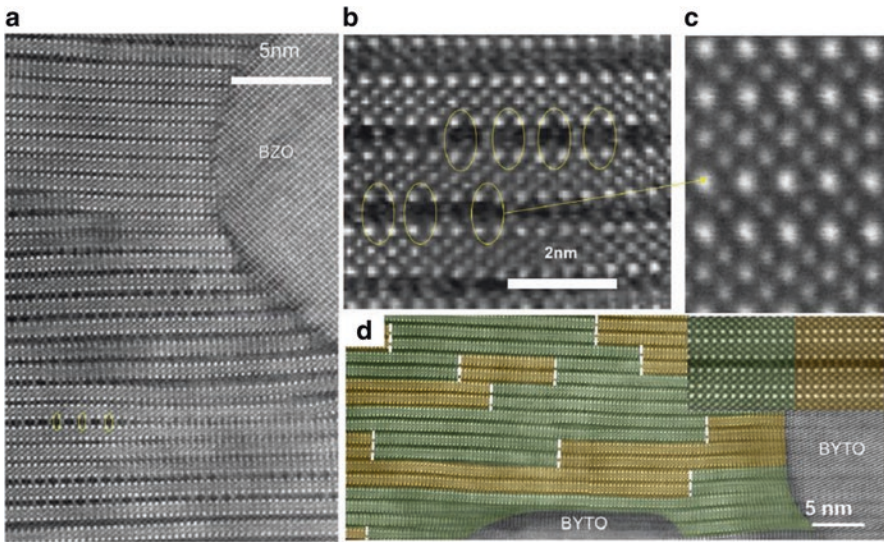


Fig. 11 High-resolution cross-sectional HAADF-TEM images of an YBCO+BZO10% nanocomposite film (a)–(c) with a large density of stacking faults, at different magnifications. (d) Twin boundary domains in a highly distorted region of an YBCO+YBTO10% nanocomposite film. Green and brown colored regions mark different twin domains, corresponding to [100] and [010] YBCO zone axes, respectively. The inset shows the magnified view of a TB. (Reproduced from Palau et al. [60])

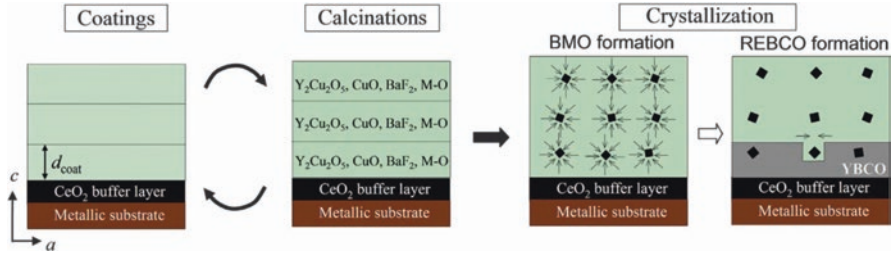


Fig. 12 Schematic diagram of the fabrication steps in Metal organic deposition (MOD) technique for the deposition of (Y,Gd)BCO films consisting of BaMO₃ (M = Zr, Hf) nanoparticles. (1) Coating a chemical solution, (2) calcination to obtain a precursor containing several amorphous phases and (3) crystallization of the superconducting phase. (Reproduced from Miura et al. [67])

In recent years, metal organic deposition (MOD) has also been evolved as a promising technique for depositing high performance REBCO superconducting thin films [64–66]. In MOD technique, the formation of secondary phase nanoinclusions takes place before host superconducting matrix formation. Figure 12 shows the schematic diagram depicting the steps of REBCO nanocomposite film growth. MOD technique consists of coatings, calcinations, and crystallization steps. The nanoparticles are formed earlier in the temperature ramp of the crystallization before the crystalline growth of the REBCO matrix, resulting in randomly distributed and oriented nanoparticles of secondary phases. This method has been demonstrated to be capable of introducing large concentrations of secondary phases which is otherwise difficult in in-situ deposition techniques. Since the crystallization process of REBCO phase in MOD technique is liquid mediated, the REBCO/APC interface is incoherent and the matrix crystalline quality is less affected as compared to in-situ techniques which allow larger concentration of secondary phase nanoinclusions.

Figure 13a shows the variation of *c*-axis length with the concentration of secondary phase nanoinclusions for PLD-grown REBCO films consisting nanocolumns, PLD-grown REBCO film consisting of nanoparticles, and MOD grown REBCO film consisting of nanoparticles as reported by Miura et al. [67]. It can be observed that while PLD-grown films exhibit elongation of the *c*-axis length for larger concentration of secondary phase nanoinclusions, MOD films keep their *c*-axis almost unaltered even for larger concentration of secondary phase nanoinclusions. The influence of intact crystalline quality of MOD REBCO films is visible in the electrical transport properties which are shown in Fig. 13b, c. The *T_c* and self-field *J_c* of the MOD grown REBCO films also do not degrade even for higher concentration of secondary phase nanoinclusions.

In order to understand the difference between the microstructures of PLD-grown and MOD grown REBCO films, high-resolution plan-view TEM images and geometrical phase analysis revealing the strain induced by secondary phase nanoinclusions in the PLD and MOD grown films are shown in Fig. 13d and e. The strain component maps reveal that in PLD-grown films, the compressive and tensile stains

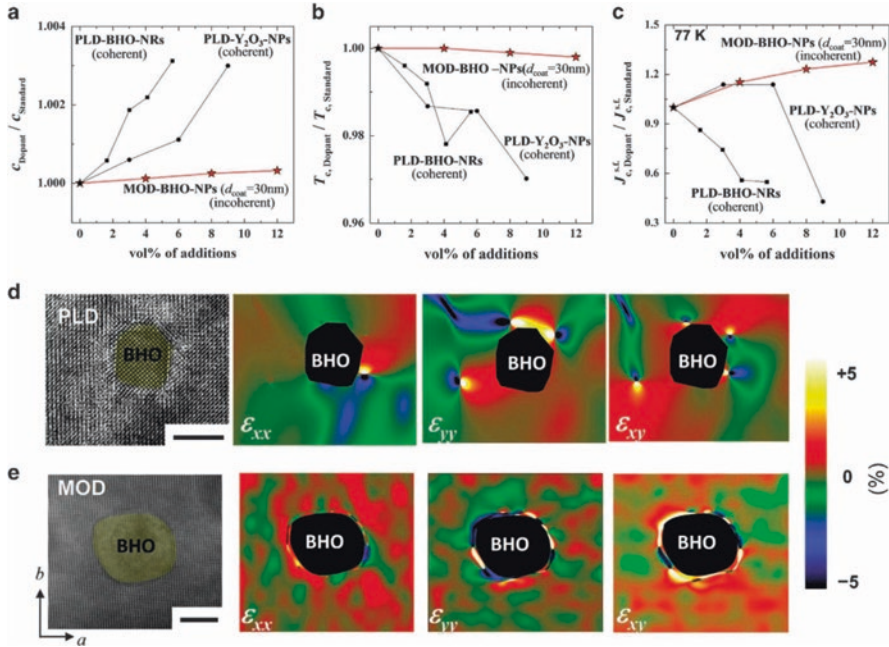


Fig. 13 Comparison of the structural and superconducting properties as a function of the concentration of secondary phase nano-inclusions and strain maps for PLD grown and MOD grown films. Variation of (a) normalized c -axis length, (b) T_c and (c) self-field J_c at 77 K as a function of the concentration of the nano-inclusions. (d) and (e) show high-resolution plan-view images, where strain (ϵ_{xx} , ϵ_{yy} , and ϵ_{xy}) maps were determined by geometrical phase analysis for PLD grown GdBCO+BHO (nanocolumns) and MOD grown (Y,Gd)BCO+BHO (nanoparticles) films. The horizontal scale bars in (d) and (e) indicate 5 nm. (Reproduced from Miura et al. [67])

are localized near the REBCO/nanocolumn coherent interfaces and spread over a distance of ~ 10 nm whereas, for MOD grown thin films, the strain is localized over far shorter distance (~ 2 nm) around the incoherent REBCO/nanoparticle interfaces. The much smaller strained regions in the REBCO matrix results in much less degradation of the superconducting properties. It has also been shown in this study that by selecting suitable secondary phase, it is possible to control the size of the nanoparticles which would result in large number of pinning sites with less deterioration of the superconducting matrix and subsequently much higher critical current performance could be realized.

6 Conclusions

In order to improve the *in-field* J_c of REBCO superconducting thin films, many methods have been tried to incorporate APCs inside REBCO film matrix. These methods have been developed over the years to intentionally introduce nanoscale secondary phases into REBCO superconducting thin films. Different secondary

phases exhibit different morphologies when incorporated in REBCO film matrix which determine the interface structures between the phases. The artificial pinning centers induced by secondary phase nanoscale inclusions and the associated interfacial strain influence the vortex pinning properties of REBCO thin films. The interfaces in REBCO superconducting thin films are governed by many parameters which include lattice misfit between the phases, surface diffusion co-efficient of adatoms, and the processing techniques. While *in-situ* fabrication techniques rely on the coherent interfaces, *ex-situ* techniques rely on incoherent interfaces for vortex pinning enhancement.

Acknowledgments We thank T. Horide, S. Saini, P. Mele, A. Ichinose, Y. Yoshida, and S. Awaji for cooperative research on vortex pinning studies in REBCO nanocomposite films.

References

1. A.P. Sutton, R.W. Balluffi, *Interfaces in Crystalline Materials* (Oxford University Press, Oxford, 1996)
2. H. Oda, S. Kiyohara, K. Tsuda, T. Mizoguchi, *J. Phys. Soc. Jpn.* **86**, 123601 (2017)
3. J.M. Howe, *Interfaces in Materials* (Wiley, New York, 1997)
4. R.W. Balluffi, S.M. Allen, W.C. Carter, *Kinetics of Materials* (Wiley, Hoboken, 2005)
5. M.K. Wu, J.R. Ashburn, C.J. Torng, P.H. Hor, R.L. Meng, L. Gao, Z.J. Huang, Y.Q. Wang, C.W. Chu, *Phys. Rev. Lett.* **58**, 908 (1987)
6. G.V.M. Williams, J.L. Tallon, *Physica C* **258**, 41 (1996)
7. M. Nakamura, H. Kutami, Y. Shiohara, *Physica C* **260**, 297 (1996)
8. J.G. Lin, C.Y. Huang, Y.Y. Xue, C.W. Chu, X.W. Cao, J.C. Ho, *Phys. Rev. B* **51**, 12900 (1995)
9. D. Larbalestier, A. Gurevich, D.M. Feldmann, A. Polyanskii, *Nature* **414**, 368 (2001)
10. A.P. Malozemoff, *Nat. Mater.* **6**, 617 (2007)
11. S.R. Foltyn, L. Civale, J.L. Macmanus-Driscoll, Q.X. Jia, B. Maiorov, H. Wang, M. Maley, *Nat. Mater.* **6**, 631 (2007)
12. D. Dijkkamp, T. Venkatesan, X.D. Wu, S.A. Shaheen, N. Jisrawi, Y.H. Min-Lee, W.L. McLean, M. Croft, *Appl. Phys. Lett.* **51**, 619 (1987)
13. X.W. Cao, X.J. Xu, Z.H. Wang, J. Fang, R.L. Wang, H.C. Li, *Physica C* **282**, 1993 (1997)
14. M. Badaye, F. Wang, Y. Kanke, K. Fukushima, T. Morishita, *Appl. Phys. Lett.* **66**, 2131 (1995)
15. B. Schey, in *Chapter 14 in "Pulsed Laser Deposition of Thin Films"*, ed. by R. Eason, (Wiley, Hoboken, 2007), pp. 313–331
16. M. Miura, in *Chapter 5 in "Oxide Thin Films, Multilayers, and Nanocomposites"*, ed. by P. Mele, T. Endo, S. Arisawa, C. Li, T. Tsuchiya, (Springer, Cham, Heidelberg, 2015), pp. 3–26
17. A. Ignatiev, in *Chapter 15 in "Second-Generation HTS Conductors"*, ed. by A. Goyal, (Kluwer Academic Publishers, Dordrecht, 2005), pp. 245–259
18. D. B. Chrisey, G. K. Hubler (eds.), *Chapter 8 in "Pulsed Laser Deposition of Thin Films"* (Wiley, New York, 1994)
19. R.K. Singh, D. Kumar, *Mater. Sci. Eng. R* **22**, 113 (1998)
20. A.K. Jha, K. Matsumoto, *Front. Phys.* **7**, 82 (2019)
21. B. Dam, J.M. Huijbregtse, F.C. Klaassen, R.C.F. Van der Geest, G. Doornbos, J.H. Rector, A.M. Testa, S. Freisem, J.C. Martinez, B. Stauble-Pumpin, R. Griessen, *Nature* **399**, 439 (1999)
22. J.M. Huijbregtse, F.C. Klaassen, A. Szepielow, J.H. Rector, B. Dam, R. Griessen, B.J. Kooi, J.T.M. de Hosson, *Supercond. Sci. Technol.* **15**, 395 (2002)
23. S.H. Wee, A. Goyal, P.M. Martin, L. Heatherly, *Supercond. Sci. Technol.* **19**, 865 (2006)

24. C. Cai, B. Holzapfel, J. Hanishch, L. Fernandez, L. Schultz, *Phys. Rev. B* **69**, 104531 (2004)
25. T. Haugan, P.N. Barnes, R. Wheeler, F. Meisenkothen, M. Sumption, *Nature* **430**, 867 (2004)
26. A.K. Jha, K. Matsumoto, T. Horide, S. Saini, P. Mele, A. Ichinose, Y. Yoshida, S. Awaji, *J. Appl. Phys.* **122**, 093905 (2017)
27. S.K. Viswanathan, A.A. Gapud, M. Varela, J.T. Abiade, D.K. Christen, S.J. Pennycook, D. Kumar, *Thin Solid Films* **515**, 6452 (2007)
28. A.K. Jha, N. Khare, R. Pinto, *Solid State Commun.* **151**, 1447 (2011)
29. J.L. MacManus Driscoll, S.R. Foltyn, Q.X. Jia, H. Wang, A. Serquis, L. Civale, B. Maiorov, M.E. Hawley, M.P. Maley, D.E. Peterson, *Nat. Mater.* **3**, 439 (2004)
30. A. Goyal, S. Kang, K.J. Leonard, P.M. Martin, A.A. Gapud, M. Varela, M. Paranthaman, A.O. Ijaduola, E.D. Specht, J.R. Thompson, D.K. Christen, S.J. Pennycook, F.A. List, *Supercond. Sci. Technol.* **18**, 1533 (2005)
31. A.K. Jha, N. Khare, R. Pinto, *J. Supercond. Nov. Magn.* **25**, 377 (2012)
32. C.V. Varanasi, J. Burke, H. Wang, J.H. Lee, P.N. Barnes, *Appl. Phys. Lett.* **93**, 092501 (2008)
33. P. Mele, K. Matsumoto, A. Ichinose, M. Mukaida, Y. Yoshida, S. Horii, R. Kita, *Supercond. Sci. Technol.* **21**, 125017 (2008)
34. S. Miura, Y. Yoshida, Y. Ichino, A. Tsuruta, K. Matsumoto, A. Ichinose, S. Awaji, *Jpn. J. Appl. Phys.* **53**, 090304 (2014)
35. S.H. Wee, A. Goyal, Y.L. Zuev, C. Cantoni, V. Selvamanickam, E.D. Specht, *Appl. Phys. Express* **3**, 023101 (2010)
36. A.K. Jha, K. Matsumoto, T. Horide, S. Saini, P. Mele, Y. Yoshida, S. Awaji, *Supercond. Sci. Technol.* **27**, 025009 (2014)
37. S.H. Wee, A. Goyal, E.D. Specht, C. Cantoni, Y.L. Zuev, V. Selvamanickam, S. Cook, *Phys. Rev. B* **81**, 140503 (2010)
38. T. Aytug, M. Paranthaman, A.A. Gapud, S. Kang, H.M. Christen, K.J. Leonard, P.M. Martin, J.R. Thompson, D.K. Christen, R. Meng, I. Rusakova, C.W. Chu, T.H. Johansen, *J. Appl. Phys.* **98**, 114309 (2005)
39. A.K. Jha, N. Khare, R. Pinto, *J. Appl. Phys.* **110**, 113920 (2011)
40. A. Gurevich, *Nat. Mater.* **10**, 255 (2011)
41. A.P. Malozemoff, T.K. Worthington, Y. Yeshurun, F. Holtzberg, P.H. Kes, *Phys. Rev. B* **38**, 7203 (1988)
42. A. Schilling, R. Jin, J.D. Guo, H.R. Ott, *Phys. Rev. Lett.* **71**, 1899 (1993)
43. H. Pastoriza, M.F. Goffman, A. Arribere, F. de la Cruz, *Phys. Rev. Lett.* **72**, 2951 (1994)
44. K. Matsumoto, P. Mele, *Supercond. Sci. Technol.* **23**, 014001 (2010)
45. X. Obradors, T. Puig, *Supercond. Sci. Technol.* **27**, 044003 (2014)
46. S. Horii, M. Haruta, A. Ichinose, T. Doi, *J. Appl. Phys.* **118**, 133907 (2015)
47. S. Horii, K. Yamada, H. Kai, A. Ichinose, M. Mukaida, R. Teranishi, R. Kita, K. Matsumoto, Y. Yoshida, J. Shimoyama, K. Kishio, *Supercond. Sci. Technol.* **20**, 1115 (2007)
48. S. Horii, H. Kai, M. Mukaida, K. Yamada, R. Teranishi, A. Ichinose, K. Matsumoto, Y. Yoshida, R. Kita, J. Shimoyama, K. Kishio, *Appl. Phys. Lett.* **93**, 152506 (2008)
49. A. Ichinose, K. Naoe, T. Horide, K. Matsumoto, R. Kita, M. Mukaida, Y. Yoshida, S. Horii, *Supercond. Sci. Technol.* **20**, 1144 (2007)
50. J. Shimoyama, K. Kitazawa, K. Shimizu, S. Ueda, S. Horii, N. Chikumoto, K. Kishio, *J. Low Temp. Phys.* **131**, 1043 (2003)
51. K. Takenaka, K. Mizuhashi, H. Takagi, S. Uchida, *Phys. Rev. B* **50**, 6534 (1994)
52. M. Namba, S. Awaji, K. Watanabe, S. Ito, E. Aoyagi, H. Kai, M. Mukaida, R. Kita, *Appl. Phys. Express* **2**, 073001 (2009)
53. T. Ozaki, Y. Yoshida, Y. Ichino, Y. Takai, A. Ichinose, K. Matsumoto, S. Horii, M. Mukaida, Y. Takano, *J. Appl. Phys.* **108**, 093905 (2010)
54. D.M. Feldmann, T.G. Holesinger, B. Maiorov, S.R. Foltyn, J.Y. Coulter, I. Apodaca, *Supercond. Sci. Technol.* **23**, 095004 (2010)
55. C. Cantoni, Y. Gao, S.H. Wee, E.D. Specht, J. Gazquez, J. Meng, S.J. Pennycook, A. Goyal, *ACS Nano* **5**, 4783 (2011)

56. B. Gautam, M.A. Sebastian, S. Chen, S. Misra, J. Huang, F.J. Baca, R. Emergo, T. Haugan, Z. Xing, H. Wang, J.Z. Wu, *Appl. Phys. Lett.* **113**, 212602 (2018)
57. J. Gutierrez, A. Llordes, J. Gazquez, M. Gibert, N. Roma, S. Ricart, A. Pomar, F. Sandiumenge, N. Mestres, T. Puig, X. Obradors, *Nat. Mater.* **6**, 367 (2007)
58. C.V. Thomson, *Annu. Rev. Mater. Sci.* **30**, 159–190 (2000)
59. J. Wu, J. Shi, *Supercond. Sci. Technol.* **30**, 103002 (2017)
60. A. Palau, F. Vallès, V. Rouco, M. Coll, Z. Li, C. Pop, B. Mundet, J. Gàzquez, R. Guzman, J. Gutierrez, X. Obradors, T. Puig, *Supercond. Sci. Technol.* **31**, 034004 (2018)
61. A. Llordes, A. Palau, J. Gazquez, M. Coll, R. Vlad, A. Pomar, J. Arbiol, R. Guzman, S. Ye, V. Rouco, F. Sandiumenge, S. Ricart, T. Puig, M. Varela, D. Chateigner, J. Vanacken, J. Gutierrez, V. Moshchalkov, G. Deutscher, C. Magen, X. Obradors, *Nat. Mater.* **11**, 329 (2012)
62. G. Deutscher, *Appl. Phys. Lett.* **96**, 122502 (2010)
63. R. Guzman, J. Gazquez, B. Mundet, M. Coll, X. Obradors, T. Puig, *Phys. Rev. Mater.* **1**, 024801 (2017)
64. M. Miura, B. Maiorov, J.O. Willis, T. Kato, M. Sato, T. Izumi, Y. Shiohara, L. Civale, *Supercond. Sci. Technol.* **26**, 035008 (2013)
65. M. Weigand, N.A. Rutter, J.H. Durrell, *Supercond. Sci. Technol.* **26**, 105012 (2013)
66. M. Miura, B. Maiorov, F.F. Balakirev, T. Kato, M. Sato, Y. Takagi, T. Izumi, L. Civale, *Sci. Rep.* **6**, 20436 (2016)
67. M. Miura, B. Maiorov, M. Sato, M. Kanai, T. Kato, T. Kato, T. Izumi, S. Awaji, P. Mele, M. Kiuchi, T. Matsushita, *NPG Asia Mater.* **9**, e447 (2017)